This is a repository copy of *An extremely low noise-equivalent power photoreceiver using high-gain InGaAs/AlGaAsSb APDs*.

White Rose Research Online URL for this paper:
https://eprints.whiterose.ac.uk/216857/

Version: Accepted Version

eprints@whiterose.ac.uk
https://eprints.whiterose.ac.uk/

An Extremely Low Noise-Equivalent Power Photoreceiver Using High-Gain InGaAs/AlGaAsSb APDs

Benjamin Sheridan, Xiao Collins, Jonathan Taylor-Mew, Benjamin White, Jo Shien Ng, *Member, IEEE,* and Chee Hing Tan, *Senior Member, IEEE*

Abstract—This work presents a high-sensitivity shortwave infrared (SWIR) photoreceiver, designed using a high-gain $In_{0.53}Ga_{0.47}As/Al_{0.85}Ga_{0.15}As_{0.56}Sb_{0.44}$ Avalanche Photodiode (APD) with an extremely low excess noise factor of <3.5 at a gain of 100. The transimpedance amplifier (TIA) and input circuitry were rigorously optimized for precise APD gain control. Under investigation with APDs of 30, 80 and 200 μm active diameters, the receiver demonstrated a record-low room-temperature Noise Equivalent Power (NEP). An extremely low NEP of 21.2 fW/√Hz was achieved with a 30-μm-diameter APD, over a 440 MHz signal bandwidth, at an APD gain of 230 and the wavelength of 1550 nm. Current commercial APD-TIA modules typically exhibit NEPs of >100 fW/√Hz to 10's of pW/√Hz. Compared to its best-in-class 80-μm counterpart, this work's receiver demonstrated a 6.5× sensitivity improvement at 2× the operating bandwidth, with an NEP of 32.5 fW/√Hz. These results are of great significance for SWIR applications including extending the range of LiDAR systems, for which optimal performance requires the maximal-sensitivity detection of few-nanosecond optical pulses. The data reported in this article is available from the ORDA digital repository (https://doi.org/10.15131/shef.data.26095804)

Index Terms—AlGaAsSb, avalanche photodiode (APD), excess noise, frequency response, high-sensitivity, noise equivalent power (NEP), optical receiver, short-wave infrared (SWIR), transimpedance amplifier (TIA).

I. INTRODUCTION

NUMEROUS applications require optical receivers capable of short-wave infrared (SWIR) detection. For many years, fiber-optic communications have exploited low-loss transmission windows at 1.3 and 1.55 μm. Lately, free-space optical communications and LiDAR applications frequently operate at wavelengths above 1 μm

Benjamin Sheridan, Jonathan Taylor-Mew, Jo Shien Ng and Chee Hing Tan are with the Department of Electronic and Electrical Engineering, The University of Sheffield, Sheffield S13JD, U.K. (e-mail: bmsheridan1@sheffield.ac.uk; j.taylor-mew@sheffield.ac.uk; j.s.ng@sheffield.ac.uk; c.h.tan@sheffield.ac.uk).

Xiao Collins and Benjamin White are with Phlux Technology Ltd., Sheffield S3 7HQ, U.K. (e-mail: xiao.collins@phluxtechnology.com; ben.white@phluxtechnology.com)

[1], [2]. LiDAR systems operating at 1550 nm offer several advantages over 905 nm systems, such as eye safety [3], longer detection ranges and improved immunity to solar irradiance [4]. Additionally, tuned 1.5-1.65 μm wavelengths are now being employed in the high-performance detection of large industrial methane leaks [5], identified as a major contributor to climate change [6]. Such LiDAR systems often use few-nanosecond pulse-widths [2], [5], demanding receiver bandwidths in the hundreds of MHz. In all cases, the receiver's sensitivity limits the smallest detectable return signal. Maximizing sensitivity not only increases detection ranges and accuracy [3], but also enables higher transmitter efficiencies [7] and improved system reliability under suboptimal conditions [8]. Whilst utilized in near-infrared applications, the spectral range of silicon detectors limits them to sub-1100 nm wavelengths. $In_{0.53}Ga_{0.47}As$ (hereafter InGaAs) SWIR detectors typically offer a detection range of 900 - 1700 nm.

The front-end of an optical receiver usually consists of a photodiode followed by a transimpedance amplifier (TIA). For high-speed and low-signal applications, the receiver's sensitivity is usually limited by the TIA's input-referred current noise. The detection of small optical signals requires careful design optimization and incurs trade-offs with speed, as increases in amplifier bandwidth are inherently accompanied by an increased noise floor. Using an avalanche photodiode (APD), the diode's avalanche multiplication gain, M, is exploited to improve the Signal-to-Noise Ratio (SNR) at the receiver's input. Under increased M, however, most APDs contribute "excess" noise due to statistical fluctuations in the multiplication gain. In the absence of any optical input, the APD's dark current, including surface and gain-multiplied bulk components, results in an APD noise floor. The latter is dependent on its excess noise factor, F, at the given M [9]. This limits the sensitivity improvements that are achievable by simply increasing M.

One useful performance metric of an optical receiver's sensitivity is that of Noise-Equivalent-Power (NEP). Defined as the optical input power required to yield a unity SNR, it is typically given in units of W/√Hz, normalized over the receiver's bandwidth. By evaluating the NEP over a range of M, the optimal APD operating point can be found at which the NEP reaches its minimum. High-performance commercial detector modules, suited for MHz-frequency SWIR applications, have so-far achieved NEPs approaching 100 fW√Hz at APD gains of M = 5–10 [10], [11], [12].

Until recently, the lowest-noise commercial SWIR APDs have generally utilized an InP or InAlAs multiplication region and an InGaAs absorber in a Separate Avalanche and Multiplication APD (SAM APD). These devices are typically operated at gains of $M \sim 10$, due to their high excess noise ($F > 5$ for $M \geq 20$) [13], [14]. There have been recent reports of very low excess noise factors from alternative avalanche materials lattice-matched to InP substrates, such as $AlAs_{0.56}Sb_{0.44}$ [15], $Al_{0.79}In_{0.21}As_{0.74}Sb_{0.26}$ [16] and $Al_{0.85}Ga_{0.15}As_{0.56}Sb_{0.44}$ [17] (hereafter AlGaAsSb). AlGaAsSb SAM APDs with a $GaAs_{0.52}Sb_{0.48}$ absorber have achieved low excess noise factors [18], [19], while Phlux Technology combined an InGaAs absorber and AlGaAsSb multiplication region to yield a low excess noise and low dark current [20], [21]. As the noise of an APD is generally the chief factor limiting its usable gain, these AlGaAsSb APDs show potential for very high gain operation, while F remains low. As such, these APDs are an interesting candidate for the design of a high-sensitivity optical SWIR receiver, in which large APD gains are employed to boost the input signal and overcome TIA noise.

In this work, a high-sensitivity SWIR detector module, with hundreds of MHz of bandwidth, was designed using linear-mode InGaAs/AlGaAsSb SAM APDs for high-gain room-temperature performance. The bandwidth, NEP and optimal-gain operating point were evaluated and compared against existing best-in-class detector modules.

II. RECEIVER DESIGN AND IMPLEMENTATION

The receiver consists of a packaged APD (TO-46) followed by a DC-coupled amplifier, as shown in Fig. 1. The design includes series protection circuitry to limit the maximum current through the APD in the event of high-power input pulses, whilst simultaneously filtering noise from the bias supply. The amplifier is composed of two stages: a TIA (LTC6563) and an output voltage buffer (MAX4444). Low-noise voltage regulators provide a filtered supply to each stage. The total gain was measured as 21 kV/A into a 50 Ω load.
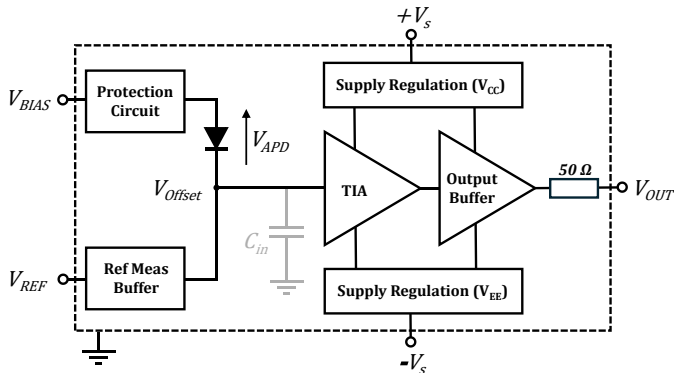

Fig. 1. Block-diagram of the receiver circuit. C_{in} represents the total parasitic capacitance seen at the input node of the TIA.

An input-side measurement buffer allows the voltage at the TIA input node (V_{Offset}) to be measured. During high-gain operation, this cathode-side reference enables precise control of the APD's

bias voltage (V_{APD}). The packaged APD is mounted via a socket in the receiver, allowing each APD to be tested in the same circuit under identical conditions. Care was taken to minimize the capacitance seen at the TIA input node (C_{in} – the sum of the APD capacitance and total stray circuit capacitance), which impacts both the TIA's bandwidth and input current noise. The entire circuit was housed in a grounded noise-shielding enclosure to mitigate the effects of electromagnetic interference (EMI). During measurements, the temperature was monitored on the package of the APD by a sheathed thermocouple probe. This was grounded at the same potential as the device's TO-46 case to mitigate higher-frequency EMI coupling.

III. EXPERIMENTAL DETAILS

The receiver performance was evaluated with commercial APDs supplied by Phlux Technology (Aura Series [20]), similar to those previously reported in [21]. These have optical-area diameters of 30, 80, and 200 μm, respectively, and are packaged in TO-46 headers.

A. Device Characterization

For each APD, dark current and capacitance versus reverse bias were measured at room temperature. Responsivity and avalanche gain were measured individually for each APD at 22.0 °C (±0.1 °C), monitored using a thermocouple probe on the device package. The 1550 nm laser source was square-wave modulated (180 Hz, 50 % duty cycle) and a lock-in amplifier used to extract the photocurrent from the dark current at low input powers. The incident optical power (25-26 nW) was measured before and after each set of responsivity readings using a calibrated power meter. Fine voltage steps at high bias were used to minimize any minor error introduced during the NEP measurement, in which linear interpolation is used to determine the bias, V_{BIAS}, required to achieve a desired value of gain. A known unity-gain responsivity value of 0.97 A/W, measured on a reference photodiode with identical InGaAs absorber thickness [21], was used to determine the gain from the responsivity data.

Excess noise was measured at room temperature by the method described in [22]. Phase-sensitive detection was used during the excess noise measurement to measure the photocurrent and noise power under illumination by a 1520 nm He-Ne laser (35 nW input power, mechanically chopped at 180 Hz). The noise was measured twice on a 200 μm device at a 10 MHz center frequency (4.4 MHz span) and evaluated against the corresponding shot noise (for the given photocurrent) measured by the calibrated setup. The gain-voltage data extracted from this measurement and the responsivity measurement are in agreement.

B. Receiver Characterization

The bandwidth and NEP of the module were measured using the setup shown in Fig. 2. APD bias was provided by a Source-Measure-Unit (SMU, Keithley 2450), operated in a 4-wire sense mode, which measured the DC input current (I_{IN}) and APD voltage (calculated from V_{SENSE}). The spectrum

analyzer was used to measure the signal response and output noise voltage (50 Ω load) across the chosen measurement bandwidth. An externally mounted peltier module ensured the entire receiver, including the APD, was maintained at 22.0 °C (±0.1 °C) throughout all NEP measurements, matching the conditions under which the gain was characterized.

For the bandwidth measurement, the continuous-wave (CW) laser source was intensity-modulated using an electro-absorption modulator (EAM, CIP 40G-SR-EAM-1550), with input RF signal of fixed modulation depth (-20 dBm AC, 50 Ω termination, -2 V_{DC} bias) provided by the tracking generator of the spectrum analyzer (Rigol DSA815-TG). The average laser power was measured as 28 nW after the EAM. The output of the receiver (V_{OUT}) was measured over the swept frequency range, providing the overall optically stimulated system frequency response. For each APD, the frequency response was measured as a function of avalanche gain, covering the full NEP-measurement gain range. These results were compared against the receiver's output noise spectra when the APD noise was dominant to reduce any uncertainties introduced by the electro-optical test fixture.
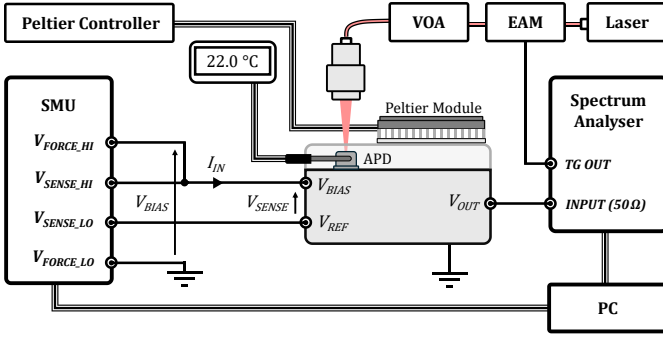

Fig. 2.   Experimental setup for frequency-response and NEP measurements.

The NEP measurement setup utilized the same setup as is shown in Fig. 2, but the APD was kept in the dark. Prior to NEP measurements, the input characteristics of the receiver circuit were evaluated using a packaged short-circuit "dummy" device (V_{APD} = 0 V in Fig. 1) under identical conditions to the actual run. The series impedance of the input circuitry and voltage offset of the cathode reference buffer were extracted by injecting bias currents over the maximum range of I_{IN}. These parameters were used to calculate the exact voltage across the APD, allowing its gain to be accurately derived during the NEP measurements.

The NEP measurement procedure was fully automated (using Standard Commands for Programmable Instruments and Python code) to minimize human error. The procedure for each reading is laid out as follows. A nominal SMU bias voltage (V_{BIAS}, Fig. 2) required to yield the desired M, is calculated using linear interpolation from each APD's pre-measured $M(V)$ data. Upon application of this bias, the software waits until the measured SMU voltage (V_{SENSE}) and current (I_{IN}) stabilize to within a defined percentage of their steady state values (<0.01 % and <3 %, respectively), ensuring any transients have settled. These values are recorded

alongside the raw output noise spectrum and total average noise voltage density (in V/√Hz) over the pre-defined measurement bandwidth. For all NEP measurements, the starting frequency (lower range of measurement bandwidth) was set at 10 Hz, corresponding to an AC-coupled receiver output. The voltage across the APD (V_{APD}) is then calculated from V_{SENSE}, I_{IN} and the measured input characteristics, accounting for the voltage drops across the reference buffer and protection circuitry. The gain and responsivity are then determined from the premeasured data. The NEP value is calculated using

$$NEP = \frac{v_{n\_out}}{G_{TIA} * R_{APD}}, \tag{1}$$

where v_{n_out} is the measured output noise density (unit: V/√Hz), G_{TIA} is the TIA's transimpedance gain (unit: V/A) and R_{APD} is the APD's responsivity including avalanche gain (unit: A/W). This procedure is repeated for different avalanche gains.

IV. RESULTS

Table I shows the room-temperature dark current at M = 10 (V_{APD} = -55 V) and device capacitance at V_{APD} = -40 V (post-punch-through) for the three diameter APDs. Both the dark current and capacitance increase with device area.

TABLE I
MEASURED ELECTRICAL CHARACTERISTICS OF EACH APD

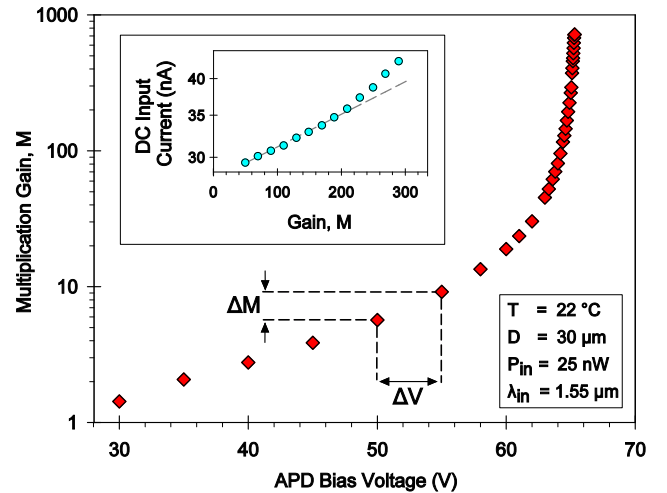| Diameter (μm)	Dark Current, I_d (nA) at M = 10	Capacitance, C_{pd} (pF) at -40 V
30	2.7	0.31
80	5.2	0.70
200	6.9	2.33

Fig. 3.   Avalanche gain versus reverse bias data of the 30-μm diameter APD. Inset shows the receiver's DC input current (I_{IN}) versus gain, measured during the 30 μm NEP run of Fig. 7. Low-gain trendline is fitted over $M \leq 200$. All measurements taken at 22.0 °C (±0.1 °C).

Fig. 3 shows the measured gain of the 30-µm diameter APD. The steepness of the gain curve (characterized by $\Delta M/\Delta V$) increases as the APD approaches breakdown. Hence it is important to maintain precise bias voltage and temperature, which can affect the gain during the NEP measurements. The inset of Fig. 3 shows the receiver's DC input current (I_{IN}) for a given M, recorded by the SMU during the 30-µm diameter NEP measurement sweep. For $M < 220$, the DC input current increases in a roughly linear fashion from its lower-gain magnitude. A rise in dark current is expected from the APD, in which the bulk leakage component increases with M. In this case, a small increase of $\Delta I_{IN} \sim 4.5$ nA is observed over $M = 100$ to 200 ($\Delta V_{BIAS} \sim 0.51$ V). For $M \geq 220$, an additional rate-of-increase in current with gain is observed. Note that the total measured I_{IN} is greater than the APD's dark current (e.g. by ~22 nA at $M = 10$). This is attributed to the finite input impedance presented by the receiver's bias circuitry to the 4-wire measurement setup.
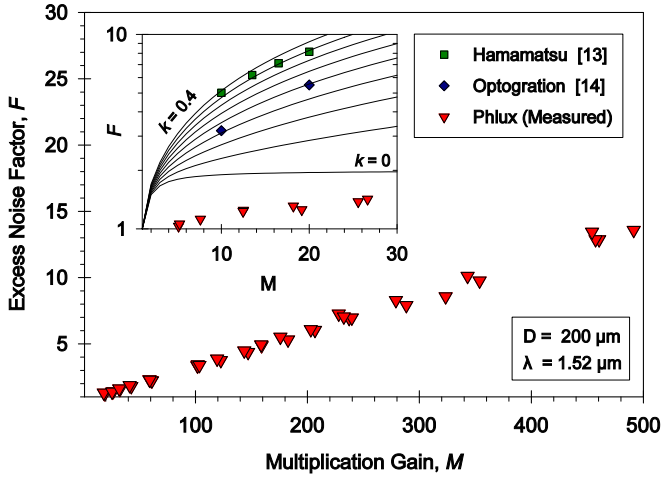
Fig. 4 shows the $F(M)$ characteristics of the 200-µm diameter APD under 1.52 µm wavelength illumination. The excess noise factor increases linearly with gain, reaching $F = 13.6$ at $M = 491$. The characteristics are much lower than those from two low-noise commercial SWIR APDs [13], [14] shown in Fig. 4 (inset). Lines indicate the $F(M)$ characteristics expected from the ionization coefficient ratio, k, in McIntyre's classical noise model [9], from 0 to 0.4, with 0.05 steps. The commercial APD characteristics correspond to $F(M)$ values typical of APDs based on InAlAs ($F_{M=10} = 3.2$, $F_{M=20} = 5.5$ for Optogration APD [14]) and InP ($F_{M=10} = 5.0$, $F_{M=20} = 8.1$ for Hamamatsu APD [13]). At $M = 100$, the excess noise of the AlGaAsSb APD ($F \sim 3.3 - 3.4$) matches that of the lowest-noise commercial InGaAs APDs operated at a much lower gain of $M = 10$ ($F \sim 3.2_{typ} - 3.7_{max}$) [14]. At a system level, this represents an order-of-magnitude improvement in the front-end signal gain with no sacrifice in excess noise.

The receiver's optical frequency response obtained with each AlGaAsSb APD, normalized to a device gain of $M = 10$, is shown in Fig. 5. Bandwidths (BW_{op}) deduced from the frequency response show no variation over the measured gain range ($M \sim 400$ for the 30 µm diameter APD and $M \sim 200$ for the other two APDs). These gain values are well beyond those recorded at the given device's NEP minimum (see later). The table in Fig. 5 shows good agreement between the measured bandwidths (BW_{op}) and those estimated from the output noise spectra (BW_n). For the 30 µm diameter APD, a $BW_{op} = 440$ MHz was obtained.

Fig. 4.   Measured excess noise factor versus gain characteristics of the 200-µm diameter APD at room temperature (two data sets). Inset compares these results against commercial InGaAs APDs [13], [14]. Reference lines plot the excess noise factors from McIntyre's equation [9] for $k = 0$ to 0.4 in 0.05 steps.
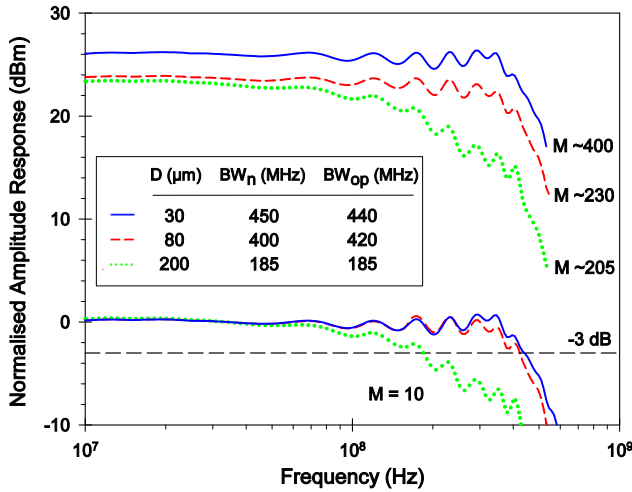

Fig. 5.   Frequency response between 10^7 and 10^9 Hz of the receiver module with each APD. Amplitude is normalized to an APD gain of $M = 10$.   Table (inset) compares BW_{op} and BW_n.
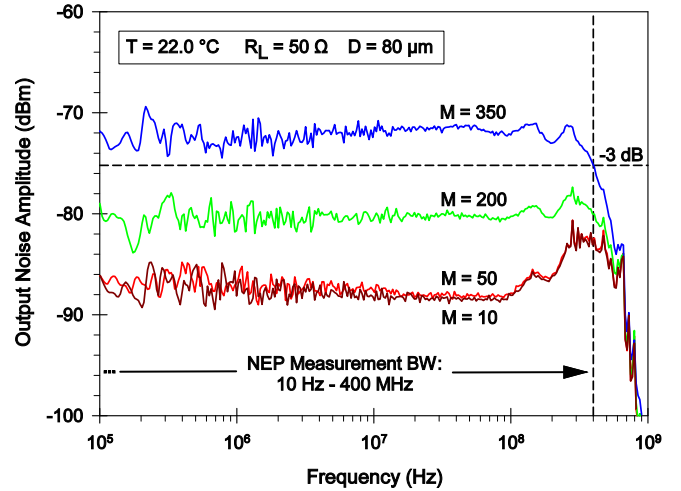

Fig. 6.   Measured output noise spectra for receiver integrated with 80-µm diameter device at increasing APD gains. Estimated -3 dB bandwidth (BW_n) of TIA shown for APD-dominated noise spectrum ($M = 350$). Noise power measured into 50 Ω load. Spectrum-analyzer resolution bandwidth of 30 kHz with RMS detection type used.

Examples of noise spectra from the 80-µm diameter APD are shown in Fig. 6. At $M = 50$, the noise is still equal to the TIA noise floor, showing no significant increase above the $M = 10$ output reference. This initial noise floor is dependent on the TIA's total input capacitance (Table I) which is, in turn, dependent on the APD capacitance. The input-referred noise value at $M = 10$ is shown in Fig. 7 (inset) and is greater for the larger-area devices. When $M = 200$ and 350, the output-noise spectrum shows the APD noise is above the TIA noise, with

the roll-off at high frequencies defined by the TIA's response. Where the bandwidth approximated from this spectrum (BW_n) differs from BW_{op} (Fig. 5 inset), the lower of the two was used as the NEP measurement bandwidth (BW_{meas}) to provide the worst-case estimation of the noise performance. In practice, choosing the larger value yielded a minimal difference in the measured noise density, with <2 % difference in the resulting NEP minimum value ($\Delta NEP_{min,30\mu m} = 0.5$ %, $\Delta NEP_{min,80\mu m} = 1.8$ %).
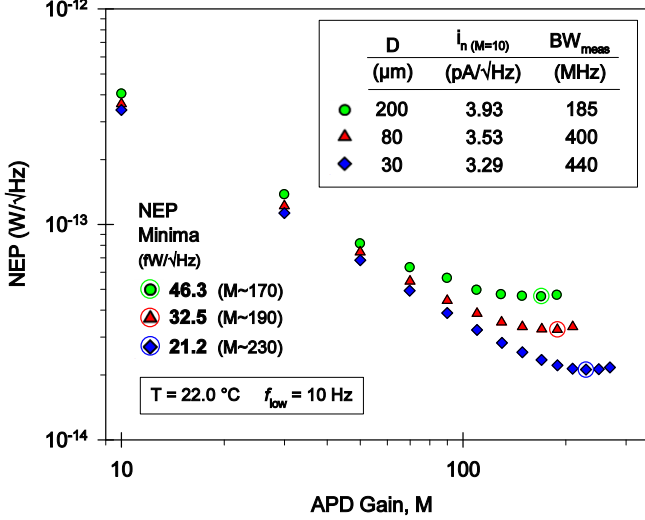

Fig. 7. NEP of the receiver versus APD gain at 22 °C when integrated with each Phlux APD. NEP minimum values are shown (bottom left) alongside the gain at which they are observed. Table (inset) shows the input-referred TIA noise (evaluated at $M = 10$) and noise-measurement upper frequency (BW_{meas}).

Fig. 7 plots the measured NEP against gain for the receiver, when integrated with each device. At lower gains ($M < 50$, for all devices), the total noise approximates to the TIA noise floor. Increasing M initially results in an inversely proportional decrease in NEP. The minimum NEP values obtained are 21.2, 32.5 and 46.3 fW/√Hz for the APDs with diameters of 30, 80 and 200 µm respectively. Thereafter, the NEP starts to rise as the APD noise contribution increases faster than the beneficial increase in M. For example, the 30-µm diameter APD's NEP increases at $M > 230$, corresponding to significant increase in the APD's dark current (inset of Fig. 3). Observing Fig. 7, the minimum NEP value occurs at higher gains for smaller-diameter devices, for which the TIA remains the dominant noise source over a larger gain range. Purposeful introduction of a temperature error (mismatch between NEP & gain measurement temps) showed a variation of less than 1 % per °C ($\Delta NEP_{min,80\mu m} = 0.6$ % / °C, $T_{meas} = 22.0 - 26.0$ °C). Estimating a worst-case compound temperature mismatch of up to 0.3 °C during the actual measurements, the resulting NEP error is calculated as <0.2 %.

V. DISCUSSION

The receiver bandwidth measured with both the 30 µm and 80 µm APDs (≥400 MHz, up to 450 MHz for 30 µm) makes it well-suited for the detection of few-ns pulse widths (≤2.5 ns).

For the 200 µm device, the lower bandwidth (185 MHz) is attributed to the higher device capacitance ($C_{pd} = 2.33$ pF). Due to the absence of circuit optimization for this specific device, the pole formed by this capacitance, in combination with the total series bias-path resistance, lies below the TIA's expected C_{in}-limited bandwidth (as can be observed by the roll-off of the 200 µm response in Fig. 6). As shown in Fig. 5, no effects on the frequency response were observed when operating at APD gains encompassing the full NEP measurement range and minima points ($M > 230$). This validates the frequency performance of the receiver at its minimum-NEP operating point. Furthermore, the absence of any bandwidth-limiting observed at even higher gains (e.g. $M \sim 400$, Fig. 5) suggests the suitability of these APDs for higher-speed applications, in which the gain-bandwidth product (GBP) of the chosen APD elsewise imposes a limitation [23], [24]. This corresponds to a GBP of beyond 170 GHz ($BW = 440$ MHz at $M \sim 400$).

The minimal variation of the measured NEP with the introduction of a temperature error (<1 % / °C) validates the reliability of the two-stage measurement procedure (<0.2 % worst-case error estimated due to any temperature mismatch). It should be noted that this is likely also benefited by the APDs' small coefficient of breakdown voltage (quoted as 20 mV/°C [20]). This temperature stability is of particular value when operating at very high gains, for which the tighter voltage-control requirements (steeper $\Delta M/\Delta V$, see Fig. 3) necessitate an increased stability of the gain-voltage characteristics.

TABLE II
NEP AND BANDWIDTH OF SWIR DETECTOR MODULES WITH VARIOUS-DIAMETER APDs

Diameter (µm)	Module	NEP (fW/√Hz)	Bandwidth (MHz)
30	This work	21.2	440
80	This work	32.5	400
	C30659-1550-R2AH [10]	220	200
200	This work	46.3	185
	C30659-1550-R2AH [10]	130	50
	CMC 264-339822-VAR [11], [12]	102	62

Table II compares this work with high-performance commercial APD modules. The 200-µm-integrated receiver here reached an NEP of 46.3 fW/√Hz over a bandwidth of 185 MHz. This is significantly better than existing modules with similar-size APDs. These are limited to NEPs of >100 fW√Hz and typically operate at $M = 5$–10 [10], [11], [12]. A module from CMC Electronics [11] was reportedly optimized to achieve an NEP of 102 fW/√Hz (1570 nm wavelength) in [12]

with a 62 MHz bandwidth. Excelitas' high-sensitivity InGaAs APD module (C30659-1550-R2AH [10]) has a quoted *NEP* = 130 fW/√Hz over a 50 MHz bandwidth.

The improved NEP performance was also observed in this work's 80-μm APD receiver, when compared to equivalent commercial modules. Excelitas' 80-μm module (C30659-1550-R2AH [10]) has a bandwidth of 200 MHz at an NEP of 220 fW/√Hz. By comparison, this 80-μm-integrated receiver demonstrated an NEP minimum of 32.5 fW/√Hz and a bandwidth of at least 400 MHz. This NEP corresponds to a factor of 6.5 improvement in sensitivity at twice the operating bandwidth of the Excelitas module.

When integrated with the 30-μm diameter APD, the receiver achieved a room-temperature NEP of 21.2 fW/√Hz over a 440 MHz bandwidth. At the time of writing, this is believed to be the lowest NEP observed for any amplifier-integrated InGaAs-APD-based detector.

To facilitate higher-frequency operation, this design has used a TIA with an input-referred noise of at least 2.9× higher than those in [10], [11], [12]. Despite this, the high-gain AlGaAsSb APDs ($M > 150$) achieve extremely low NEPs. Further improvements can be expected for optimizations of the design, including the reduction of layout parasitics and elimination of the APD test receptacle ($C_{para} \sim 0.7$ pF).

VI. CONCLUSION

This work presented a high-sensitivity SWIR photoreceiver, designed using low-noise InGaAs/AlGaAsSb APDs. The receiver included input bias circuitry which was carefully characterized to enable precise high-gain APD operation. It was tested at room temperature with APDs of 30, 80 and 200 μm diameters and its performance was compared against existing commercial modules. The receiver demonstrated an extremely low NEP of 21.2 fW/√Hz, over a 440 MHz signal bandwidth, using a 30 μm APD at a gain of $M = 230$. Frequency-response measurements showed no bandwidth limiting at measured gains well beyond this NEP minima (M ~ 400), evidencing an APD gain-bandwidth product exceeding 170 GHz. These results evidence the practical capability of these APDs to be operated with low excess noise at very high gains, greatly improving the front-end SNR to overcome amplifier noise. This is of significance for SWIR applications requiring the detection of heavily attenuated return signals, whilst maintaining reasonable bandwidths.

ACKNOWLEDGMENT

REFERENCES

[1] E. Leitgeb *et al.*, "Analysis and evaluation of optimum wavelengths for free-space optical transceivers," in *2010 12th International Conference on Transparent Optical Networks*, Munich, Germany: IEEE, Jun. 2010, pp. 1–7. doi: 10.1109/ICTON.2010.5549009.

[2] P. F. McManamon, *LiDAR technologies and systems*. Bellingham, Washington, USA: SPIE Press, 2019.

[3] Z. Dai, A. Wolf, P.-P. Ley, T. Glück, M. C. Sundermeier, and R. Lachmayer, "Requirements for Automotive LiDAR Systems," *Sensors*, vol. 22, no. 19, p. 7532, Oct. 2022, doi: 10.3390/s22197532.

[4] H. Willebrand and B. S. Ghuman, *Free Space Optics: Enabling Optical Connectivity in Today's Networks*. Sams Publishing, 2002.

[5] J. Titchener *et al.*, "Single photon Lidar gas imagers for practical and widespread continuous methane monitoring," *Appl. Energy*, vol. 306, p. 118086, Jan. 2022, doi: 10.1016/j.apenergy.2021.118086.

[6] Intergovernmental Panel On Climate Change (Ipcc), *Climate Change 2021 – The Physical Science Basis: Working Group I Contribution to the Sixth Assessment Report of the Intergovernmental Panel on Climate Change*, 1st ed. Cambridge University Press, 2023. doi: 10.1017/9781009157896.

[7] J. N. Hansen *et al.*, "Assessing Novel Lidar Modalities for Maximizing Coverage of a Spaceborne System through the Use of Diode Lasers," *Remote Sens.*, vol. 14, no. 10, p. 2426, May 2022, doi: 10.3390/rs14102426.

[8] R. H. Rasshofer, M. Spies, and H. Spies, "Influences of weather phenomena on automotive laser radar systems," *Adv. Radio Sci.*, vol. 9, no. B.2, pp. 49–60, Jul. 2011, doi: 10.5194/ars-9-49-2011.

[9] R. J. McIntyre, "Multiplication noise in uniform avalanche diodes," *IEEE Trans. Electron Devices*, vol. ED-13, no. 1, pp. 164–168, Jan. 1966, doi: 10.1109/T-ED.1966.15651.

[10] Excelitas, "Si and InGaAs APD Preamplifier Modules." C30659 Series Datasheet, Apr. 2023. Accessed: May 01, 2024. [Online]. Available: https://www.excelitas.com/product/c30659-1550-r2ah-ingaas-apd-receiver-200um-8-50mhz

[11] CMC Electronics, "Dual Wavelength InGaAs Avalanche Photodiode Preamplifier Module." CMC-MEG-INGAAS-21-001 Datasheet. Accessed: May 01, 2024. [Online]. Available: https://cmcelectronics.ca/wp-content/uploads/2024/01/4.5.2-flyer-InGaAs-21-001-264-339814.pdf

[12] P. Lepage, J.-F. Rioux, P. Verville, E. Talbot, N. Belanger, and B. Fong, *High gain, low noise InGaAs APD receiver with fast overload recovery and stable performance through wide temperature range*, vol. 12008. in Photonic Instrumentation Engineering IX., vol. 12008. SPIE, 2022. doi: 10.1117/12.2603212.

[13] Hamamatsu, "InGaAs APD." G8931 Series Datasheet, Jul. 2019. Accessed: May 01, 2024. [Online]. Available: https://www.hamamatsu.com/content/dam/hamamatsu-photonics/sites/documents/99_SALES_LIBRARY/ssd/g8931_series_kapd1018e.pdf

[14] Optogration, "Avalanche Photodiodes." OG-AP-080-12 Datasheet. Accessed: May 01, 2024. [Online]. Available: https://optogration.com/specifications

[15] X. Yi *et al.*, "Demonstration of large ionization coefficient ratio in AlAs$_{0.56}$Sb$_{0.44}$ lattice matched to InP," *Sci. Rep.*, vol. 8, no. 1, p. 9107, Jun. 2018, doi: 10.1038/s41598-018-27507-w.

[16] S. H. Kodati *et al.*, "AlInAsSb avalanche photodiodes on InP substrates," *Appl. Phys. Lett.*, vol. 118, no. 9, p. 091101, Mar. 2021, doi: 10.1063/5.0039399.

[17] J. Taylor-Mew, V. Shulyak, B. White, C. H. Tan, and J. S. Ng, "Low Excess Noise of Al$_{0.85}$Ga$_{0.15}$As$_{0.56}$Sb$_{0.44}$ Avalanche Photodiode From Pure Electron Injection," *IEEE Photonics Technol. Lett.*, vol. 33, no. 20, pp. 1155–1158, Oct. 2021, doi: 10.1109/LPT.2021.3110123.

[18] Y. Cao, T. Blain, J. D. Taylor-Mew, L. Li, J. S. Ng, and C. H. Tan, "Extremely low excess noise avalanche photodiode with GaAsSb absorption region and AlGaAsSb avalanche region," *Appl. Phys. Lett.*, vol. 122, no. 5, p. 051103, Jan. 2023, doi: 10.1063/5.0139495.

[19] Y. Liu *et al.*, *Very high gain and low noise GaAsSb/AlGaAsSb avalanche photodiodes for 1550nm detection at room temperature*, vol. 12882. in Optical Components and Materials XXI., vol. 12882. SPIE, 2024. doi: 10.1117/12.3011687.

[20] Phlux Technology Ltd, "Noiseless InGaAs™ APDs." Aura Series 80 μm Datasheet. Accessed: May 01, 2024. [Online]. Available: https://phluxtechnology.com/products/aura-noiseless-ingaas-apds#datasheets

[21] X. Collins *et al.*, "Low-noise AlGaAsSb avalanche photodiodes for 1550nm light detection," in *Optical Components and Materials XIX*, SPIE, Mar. 2022, pp. 51–56. doi: 10.1117/12.2608842.

[22] K. Lau *et al.*, "Excess noise measurement in avalanche photodiodes using a transimpedance amplifier front-end," *Meas. Sci. Technol.*, vol. 17, p. 1941, Jun. 2006, doi: 10.1088/0957-0233/17/7/036.

[23]   M. Nada, Y. Yamada, and H. Matsuzaki, "Responsivity-Bandwidth
        Limit of Avalanche Photodiodes: Toward Future Ethernet Systems,"
        IEEE J. Sel. Top. Quantum Electron., vol. 24, no. 2, pp. 1–11, Mar.
        2018, doi: 10.1109/JSTQE.2017.2754361.
[24]   M. Nada, T. Yoshimatsu, F. Nakajima, H. Matsuzaki, and K. Sano,
        "High-speed Avalanche Photodiodes toward 100-Gbit/s per Lambda
        Era," *NTT Tech. Rev.*, vol. 16, no. 11, pp. 45–51, Nov. 2018, doi:
        10.53829/ntr201811ra1.